RESEARCH ARTICLE

Correspondence to:
X. Liu,
liuxiao@htu.edu.cn

Variations of global gravity waves derived from 14 years of SABER temperature observations

Xiao Liu[1,2] (iD), Jia Yue[3,4] (iD), Jiyao Xu[2,5] (iD), Rolando R. Garcia[6] (iD), James M. Russell III[3] (iD), Martin Mlynczak[7] (iD), Dong L. Wu[8] (iD), and Takuji Nakamura[9] (iD)

[1]Henan Engineering Laboratory for Big Data Statistical Analysis and Optimal Control, School of Mathematics and Information Sciences, Henan Normal University, Xinxiang, China, [2]State Key Laboratory of Space Weather, National Space Science Center, Chinese Academy of Sciences, Beijing, China, [3]Atmospheric and Planetary Sciences, Hampton University, Hampton, Virginia, USA, [4]ESSIC, University of Maryland, College Park, Maryland, USA, [5]College of Earth Science, University of the Chinese Academy of Science, Beijing, China, [6]Atmospheric Chemistry Observations and Modeling Laboratory, National Center for Atmospheric Research, Boulder, Colorado, USA, [7]NASA Langley Research Center, Hampton, Virginia, USA, [8]Climate and Radiation Laboratory, NASA Goddard Space Flight Center, Greenbelt, Maryland, USA, [9]National Institute of Polar Research, Tachikawa, Japan

Abstract The global gravity wave (GW) potential energy (PE) per unit mass is derived from SABER (Sounding of the Atmosphere using Broadband Emission Radiometry) temperature profiles over the past 14 years (2002–2015). Since the SABER data cover longer than one solar cycle, multivariate linear regression is applied to calculate the trend (means linear trend from 2002 to 2015) of global GW PE and the responses of global GW PE to solar activity, to QBO (quasi-biennial oscillation) and to ENSO (El Niño–Southern Oscillation). We find a significant positive trend of GW PE at around 50°N during July from 2002 to 2015, in agreement with ground-based radar observations at a similar latitude but from 1990 to 2010. Both the monthly and the deseasonalized trends of GW PE are significant near 50°S. Specifically, the deseasonalized trend of GW PE has a positive peak of 12–15% per decade at 40°S–50°S and below 60 km, which suggests that eddy diffusion is increasing in some places. A significant positive trend of GW PE near 50°S could be due to the strengthening of the polar stratospheric jets, as documented from Modern Era Retrospective-analysis for Research and Applications wind data. The response of GW PE to solar activity is negative in the lower and middle latitudes. The response of GW PE to QBO (as indicated by 30 hPa zonal winds over the equator) is negative in the tropical upper stratosphere and extends to higher latitudes at higher altitudes. The response of GW PE to ENSO (as indicated by the Multivariate ENSO Index) is positive in the tropical upper stratosphere.

Plain Language Summary Gravity waves (GWs) are disturbances of the atmosphere with horizontal wavelengths of several kilometers to several thousand kilometers. GWs can be generated by many sources, e.g., wind jets, deep convection, and flow over topography. The global GW potential energy (PE) per unit mass is derived from SABER (Sounding of the Atmosphere using Broadband Emission Radiometry) temperature profiles over the past 14 years (2002–2015). We find a significant positive trend of GW PE at around 50°N during July from 2002 to 2015. Both the monthly and the deseasonalized trends in of GW PE are significant near 50°S. Specifically, the deseasonalized trend of GW PE has a positive peak of 12–15% per decade at 40°S–50°S and below 60 km, which suggests that eddy diffusion is increasing in some places. The response of GW PE to solar activity is negative in the lower and middle latitudes. The response of GW PE to QBO (as indicated by 30 hPa zonal winds over the equator) is negative in the tropical upper stratosphere and extends to higher latitudes at higher altitudes. The response of GW PE to ENSO (as indicated by the MEI index) is positive in the tropical upper stratosphere.

1. Introduction

Gravity waves (GWs) are disturbances of the atmosphere with horizontal wavelengths of several kilometers to several thousand kilometers. GWs can be generated by many sources, e.g., wind jets, deep convection, and flow over topography [*Fritts and Alexander*, 2003]. The propagation of GWs is influenced by the environment (background wind and atmospheric stability) [*Nappo*, 2002]. When GWs break, the momentum and energy they carry from the source region are deposited into the mean flow and thus influence the local

atmospheric structure and even the global atmospheric circulation [*Lindzen*, 1981; *Holton*, 1983]. Meanwhile, breaking GWs can enhance the local eddy diffusion and influence the local distribution of atmospheric species [*Liu et al.*, 1999; *Xu et al.*, 2006]. Thus, GW effects have to be included in general circulation models (GCMs) to reproduce realistic atmospheric structures [*Kim et al.*, 2003; *Alexander et al.*, 2010].

A recent study by *Yue et al.* [2015] has shown that there is a positive trend of CO_2 derived from 13 years (2002–2014) of SABER (Sounding of the Atmosphere using Broadband Emission Radiometry) observations, consistent with the trend derived by *Emmert et al.* [2012] from 11 years (2004–2014) of ACE-FTS (Atmospheric Chemistry Experiment Fourier Transform Spectrometer) observations. Moreover, the positive trend increases with height above 80 km in both SABER and ACE-FTS data. However, the positive trend in CO_2 derived from WACCM (Whole Atmosphere Climate Community Model) is essentially constant with altitude, and no larger than the rate of increase attributable to anthropogenic emissions [*Garcia et al.*, 2016]. *Emmert et al.* [2012] showed that the increasing CO_2 in the mesosphere and lower thermosphere could be reproduced by increasing the vertical eddy diffusion coefficient by 15% per decade in the 1-D model of *Roble* [1995], while *Garcia et al.* [2016] estimated that a 30% per decade increase would be necessary in WACCM (but the model did not produce any trend in this quantity over the last couple of decades). According to linear GW saturation theory, the eddy diffusion induced by GWs is proportional to the fourth power of the intrinsic phase speed; the wave energy of breaking GWs is proportional to the square of the intrinsic phase speed [*Lindzen*, 1981]. Thus, the wave energy and therefore the amplitude of breaking GWs are strongly related to the GW-induced eddy diffusion. GWs and the associated eddy diffusion cannot be resolved explicitly in a GCM given current computing capacity and are instead parameterized. As computational technology and capacity have increased, GCMs can be run at sufficiently high horizontal resolution to resolve GWs, but the computational costs make calculations over long periods impractical at this time [*Watanabe et al.*, 2008; *H.-L. Liu et al.*, 2014; *Holt et al.*, 2016]. Thus, it is compelling to study the variations of GWs observationally.

Observations provide realistic information on the spatial (e.g., latitude, longitude, and height) and temporal (e.g., monthly, seasonal, and long-term) distributions of GWs and enable us to provide some constraints on GW parameterizations in GCMs. Satellite observations are valuable complements to conventional ground-based and in situ observations of GWs, especially as regards the global distribution of GWs. Thus, it is important to characterize the global GWs based on satellite observations.

Fetzer and Gille [1994] interpreted the wave-like structures in temperature profiles from the LIMS (Limb Infrared Monitor of the Stratosphere) satellite experiment as low-frequency (inertia) GWs. Subsequently, many researchers have made efforts to analyze the global distribution of GWs based on satellite observations. *Wu and Waters* [1996] explained the small-scale temperature fluctuations observed by the MLS (Microwave Limb Sounder) instrument on board the UARS (Upper Atmosphere Research Satellite) as propagating high-frequency GWs (with horizontal wavelength less than ~100 km) in the middle atmosphere. These high-frequency GWs were strongly related to tropospheric convection (over equatorial and middle latitude land masses), surface topography (at middle latitudes), and stratospheric jet streams (in polar regions). Due to different observational techniques used in different satellite instruments, the observed GWs have different frequencies or wavelengths. *Wu and Eckermann* [2008] classified the GWs observed by satellites into three types: (1) the MLS instruments on board UARS and on the Earth Observing System (EOS) Aura satellite are sensitive to GWs with high intrinsic frequencies; (2) the limb sounders, e.g., LIMS, SABER, CRISTA (Cryogenic Infrared Spectrometers and Telescopes for the Atmosphere), and HIRDLS (High Resolution Dynamics Limb Sounder) are sensitive to GWs with low frequencies [*Fetzer and Gille*, 1994; *Tsuda et al.*, 2000; *Preusse et al.*, 2002, 2006; *Ern et al.*, 2004; *Alexander et al.*, 2008; *Wang and Alexander*, 2010; *Alexander*, 2015]; and (3) similar to MLS-like instruments, nadir sounders (e.g., Advanced Microwave Sounding Unit A and Atmospheric Infrared Sounder) are sensitive to GWs with high frequencies. However, compared to MLS-like instruments, the sensitivity of nadir sounders covers also somewhat shorter horizontal scales [*Wu*, 2004; *Alexander and Barnet*, 2007; *Yue et al.*, 2013, 2014; *Gong et al.*, 2015; *Sato et al.*, 2016; *Tsuchiya et al.*, 2016]. The global distributions of GWs and their temporal variations can be studied based on these satellite observations.

Using the MLS/UARS observations from 1991 to 1997, *Jiang et al.* [2005, 2006] showed that the high-latitude (45°N/S–65°N/S) GWs exhibit annual variations with peak in winter and trough in summer in the stratosphere; in the mesosphere, GWs exhibit a semiannual variation with peaks in both winter and summer. The interannual variations of GWs at high latitudes are correlated with the strength of the polar vortex. In the subtropical

region (45°S–45°N), the convectively generated GWs are dominant in the summer stratosphere. Despite different methods of extracting GWs from the temperature profiles used by SABER, HIRDLS, and CRISTA and the different temporal coverage of these instruments, GWs show clear semiannual, annual, and biennial variations [e.g., *Krebsbach and Preusse*, 2007; *Ern et al.*, 2011, 2014, 2015; *Zhang et al.*, 2012]. Studying the longer-term (e.g., decadal and solar cycle) changes of GWs is challenging because of the limited temporal extension of the observation data.

Until now the variations of GWs have only been explored using ground-based observations with a temporal coverage of more than 10 years [e.g., *Gavrilov et al.*, 1995, 2002, 2004; *Jacobi et al.*, 2006; *Li et al.*, 2010; *Hoffmann et al.*, 2011]. By analyzing GWs derived from medium frequency (MF) radar winds at Saskatoon (52°N, 107°W) from 1979 to 1993, *Gavrilov et al.* [1995] found that there is a negative correlation between GWs and 11 year solar cycle activity. We note that the solar cycle activity is represented by solar radiation flux at 10.7 cm ($F_{10.7}$). By analyzing the GWs at three stations (Saskatoon: 52°N, 107°W; Collm: 52°N, 15°E; and Shigaraki: 35°N, 136°E), *Gavrilov et al.* [2002] noted that the correlation between GWs and solar activity is dependent on longitude. By analyzing the GWs derived from MF radar winds at Hawaii (22°N, 160°W) from 1990 to 2000, *Gavrilov et al.* [2004] found that enhanced GWs in the mesosphere might be caused by enhanced GW sources in the lower atmosphere during strong El Niño events. By analyzing the GWs derived from the half-hourly mean drift velocities at Collm (52°N, 13°E) from 1984 to 2003, *Jacobi et al.* [2006] found a positive correlation between GWs and solar activity, which is inconsistent with the negative correlation between GWs and solar activity at Saskatoon [*Gavrilov et al.*, 1995]. Although *Jacobi et al.* [2006] ascribed this inconsistency to the stronger westward jet in the mesosphere during solar maximum, they did not exclude other factors (e.g., ionospheric perturbations and GW sources) that could influence solar cycle variations of GWs. Using a 10.5 year temperature data set derived from Rayleigh lidar at Hawaii (19.5°N, 155.6°W), *Li et al.* [2010] showed that there is an enhancement of GW temperature variance during the solar maximum in 2000–2002 in the upper stratosphere, but such an enhancement is not clear in the lower mesosphere. Using the MF radar wind data at Juliusruh (55°N, 13°E) from 1990 to 2010, *Hoffmann et al.* [2011] showed that the GWs with periods of 3–6 h in July exhibit a positive trend of 0.6–1.8 m^2 s^{-2} per year above 80 km, which is anticorrelated with the more westward zonal wind trend underneath, at about 75 km. The anticorrelation between GWs and zonal winds might be due to the selective GW filtering by the background since the eastward propagating GWs are stronger than the westward propagating GWs during summer months [*Hoffmann et al.*, 2011]. These ground-based observations shed some light on the variations of GWs and their possible relations with solar activity, El Niño, and zonal-mean wind. However, the global variations of GWs over more than 10 years are also an important issue and should be studied.

Because of their long-duration, SABER observations provide a good opportunity to study the global variation of GWs over the period from 2002 to 2015. GWs extracted from SABER temperature profiles exhibit variability on several time scales: annual, semiannual, quasi-biennial, and 11 year (the latter presumably related to the 11 year solar activity cycle) [e.g., *Ern et al.*, 2011; *John and Kumar*, 2012; *Zhang et al.*, 2012]. Using the SABER temperature data from 2002 to 2011, *Ern et al.* [2011] showed that the GW amplitude and momentum flux are stronger in the years 2008–2009 than in the years 2002–2003 and 2010–2011. They indicated that the GW amplitude and the magnitude of momentum flux might be anticorrelated with solar activity (indicated by the solar radio flux at 10.7 cm, $F_{10.7}$). As noted by *Ern et al.* [2011], the 9 year data set is too short to discriminate unambiguously between long-term trends and solar activity dependence of global GWs. Now the SABER temperature data extend from 2002 to 2015, which is longer than one solar cycle. Thus, the focus of this work is to study the long-term variations of GWs and their response to solar activity, QBO (quasi-biennial oscillation) and ENSO (El Niño–Southern Oscillation).

The remainder of this paper is organized as follows. In section 2 the data sets (SABER temperature data and the reference time series used for regression analyses) and methods of extracting GWs and multivariate linear regression (MLR) are described. The global climatology of GWs (latitude, height, and temporal variations) is presented in section 3. The long-term changes of GWs and their comparisons with other studies are given in section 4. In section 5 we present the GW responses to solar activity, QBO, and ENSO. Our discussions on the trends of GWs are given in section 6. Finally, a summary is given in section 7. A detailed description of GW extraction method is given in Appendix A.
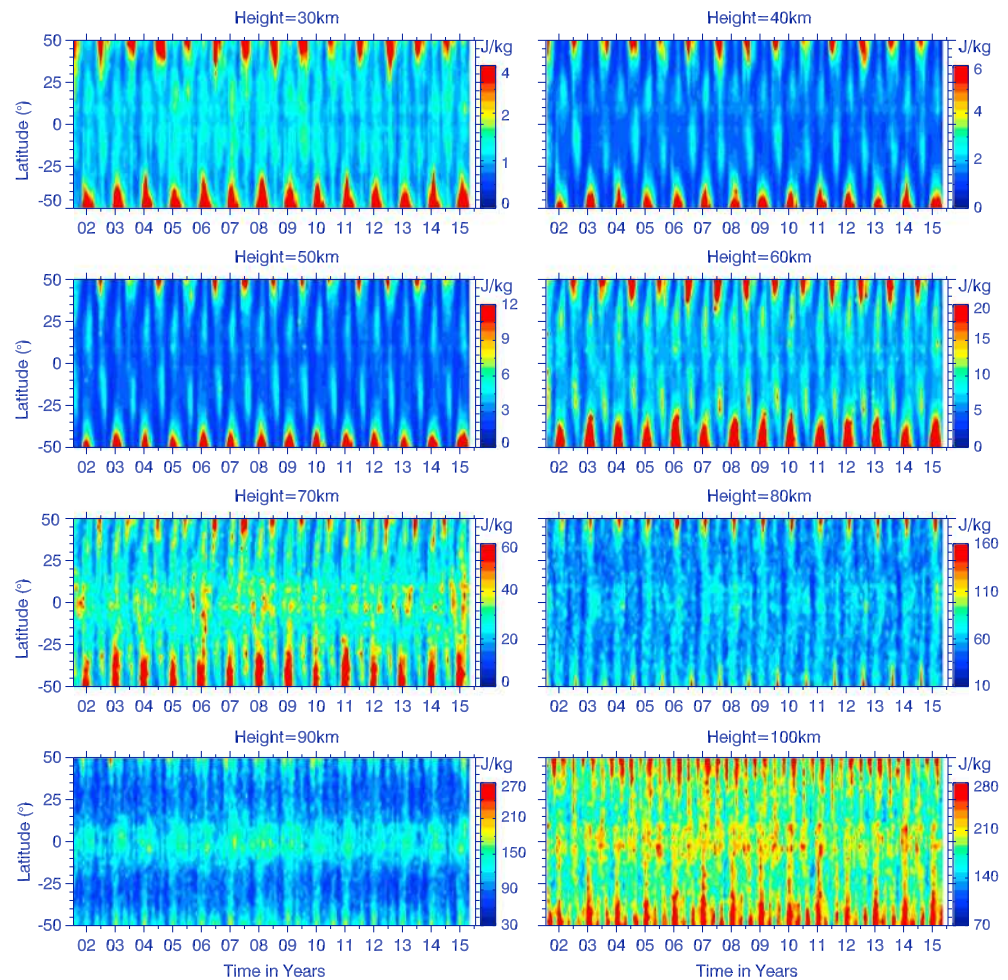
Figure 1. Latitude-time sections of the monthly and zonal-mean GW potential energy (PE) at several heights (from 30 km to 100 km with height interval of 10 km). The labeled tick year marks the 15 June of each year.

2. Data and Method

2.1. SABER Temperature

The TIMED (Thermosphere Ionosphere Mesosphere Energetics and Dynamics) satellite was launched into an orbit with height of 625 km and inclination of 74.1° on 7 December 2001. The SABER instrument [*Russell et al.*, 1999] on board the TIMED satellite has measured temperature and several trace species profiles from ~20 km to ~110 km since January of 2002. The latitude coverage shifts from 53°N–83°S to 53°S–83°N due to the yaw cycle of ~60 days (yaw maneuvers are necessary so that the radiometer never looks directly at the Sun). The SABER temperature retrieval procedure and validation have been reported by *Remsberg et al.* [2008, and references therein]. Because SABER uses the limb-scanning measurement technique, SABER observations are sensitive to GWs with horizontal and vertical wavelengths longer than ~100–200 km and ~4 km, respectively [*Preusse et al.*, 2002].

In this work, SABER temperature profiles (V2.0, Level 2A) are used to extract GWs. Then the long-term variations of GWs could be resolved since SABER data have covered 14 years (from 2002 to 2015).

2.2. Method of Extracting GW

The GW extraction method used here is similar to that proposed by *Fetzer and Gille* [1994], *Preusse et al.* [2002, 2009], *Yamashita et al.* [2013], and *X. Liu et al.* [2014]. The detailed procedure for extracting GWs from SABER temperature profiles is given in Appendix A. Figure 1 shows the monthly and zonal-mean GW potential
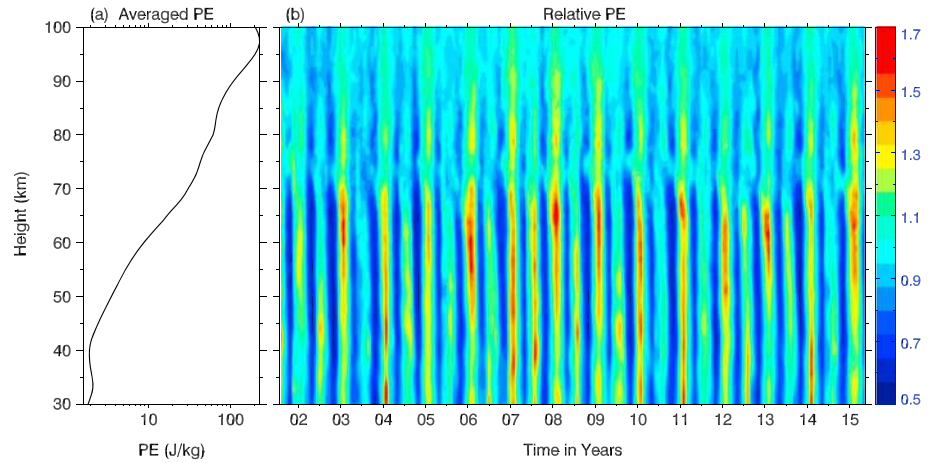
Figure 2. (a) Profile of all years and globally (50°S–50°N) averaged gravity wave potential energy. (b) Latitude-time section of relative GW PE (RPE). The relative GW PE is calculated by dividing the monthly and global (50°S–50°N) mean GW PE by the all-year average of global mean GW PE shown in Figure 2a. The unit of color bar is RPE. The labeled tick marks the 15 June of each year.

energy per unit mass (PE) as a function of month and latitude at heights of 30–100 km with height interval of 10 km. We note that the monthly GW PE is calculated by averaging the daily GW PE within a single month.

GW PE per unit mass is proportional to the squared perturbation temperature (see equation (A1) of Appendix A) and increases with height exponentially since atmospheric density decreases with height exponentially. To make the temporal variation of GW PE more visible across a wide range of altitude, we use the relative GW PE (RPE), which is defined as RPE = PE/<PE>, where <PE> is the time-mean PE at each height. Figure 2 shows the time-mean global-mean GW PE (Figure 2a) and the monthly global-mean RPE (Figure 2b). In a same way we get the monthly zonal-mean RPE by dividing the time-mean zonal-mean PE from the monthly zonal-mean PE at each latitude. Figure 3 shows the RPE at several latitudes of the Northern (left) and Southern (right) Hemispheres. The general features of the global GWs and their temporal and height variations will be described in the next section.

2.3. Method of Extracting Long-Term Changes

The monthly zonal-mean RPE at a given height is binned into a box of 20° × 5° (longitude times latitude) having overlap of 10° in longitude and 2.5° in latitude. Then the linear trend of RPE and the responses of RPE to solar activity, QBO wind, and ENSO are calculated by multivariate linear regression (MLR). The MLR equation is expressed as

$$\text{RPE}(t_{i,j}) = \mu + \alpha \cdot t_{i,j} + \beta \cdot \text{solar}(t_{i,j}) + \gamma \cdot \text{QBO}(t_{i,j}) + \kappa \cdot \text{ENSO}(t_{i,j}) + \text{Residual, with } i = 2002, 2003, \ldots, 2015, j = 1, 2, \ldots, 12. \tag{1}$$

In equation (1), RPE($t_{i,j}$) is the time series at month (*j*) and year number (*i*) from 2002 to 2015. The quantity μ represents a constant RPE. Then, we can get a linear trend (α) and responses of RPE to solar activity (β), QBO (γ), and ENSO (κ) at month (*j*) by varying the year (*i*) from 2002 to 2015 in equation (1). We note that the linear trend of RPE and the responses of RPE to solar activity, QBO, and ENSO derived here are valid for the SABER data from 2002 to 2015. Since RPE = PE/<PE> and <PE> is the time mean at any given level, the linear trend in RPE, α, is simply the trend in PE relative to its time mean. Multiplying α times 100% then gives the percentage trend relative to its time mean. In the same way, one can get percentage responses of PE to solar activity, QBO, and ENSO. The confidence levels for the fitted coefficients are estimated according to the variance–covariance matrix [see *Kutner et al.*, 2004, chapter 6] and the student *t* test [see *Kutner et al.*, 2004, chapter 2].

Since SABER sampling is discontinuous at latitudes poleward of 55°S–55°N due to the yaw cycle, we restrict the results to the latitude band of 50°S–50°N, where the SABER data sampling is continuous. Over this
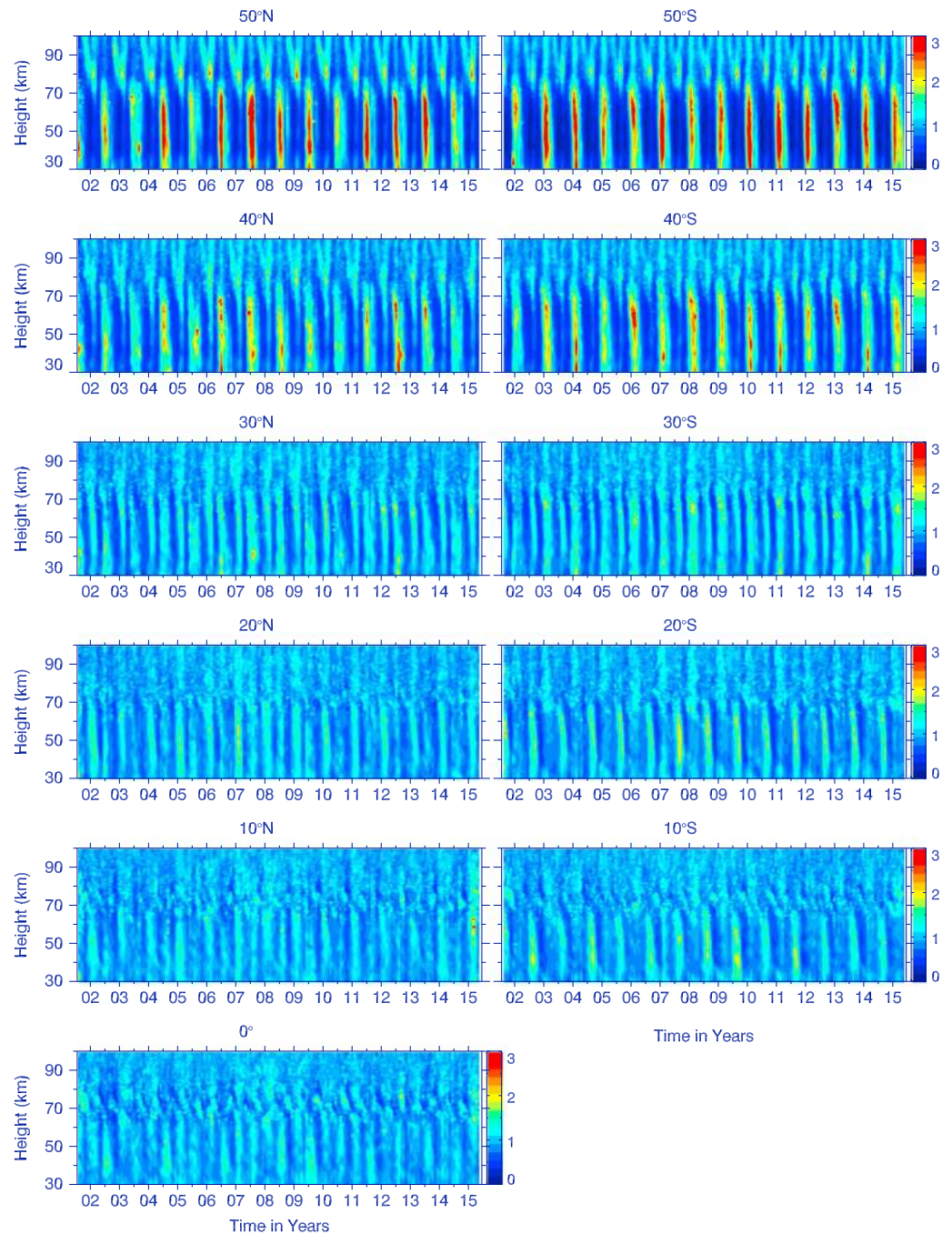
Figure 3. Time-height sections of the RPE at several latitudes of the (left column) Northern and (right column) Southern Hemispheres. The RPE is calculated by dividing the monthly zonal-mean GW PE by the all-year zonal-mean GW PE. The unit of color bar is RPE. The labeled tick marks the 15 June of each year.

latitude range, we can obtain reliable long-term changes of GWs and their responses to solar activity, QBO, and ENSO.

The reference time series of solar activity is the solar radio flux at 10.7 cm ($F_{10.7}$), shown in Figure 4a in solar flux units (sfu), where 1 sfu $= 10^{-22}$ W m^{-2} Hz^{-1} [*Tapping*, 2013]. The reference time series for the QBO is the 30 hPa zonal-mean zonal wind at the equator and is shown in Figure 4b [*Baldwin et al.*, 2001]. The reference time series for ENSO is the Multivariate ENSO Index (MEI), shown in Figure 4c [*Randel et al.*, 2009; *Wolter and Timlin*, 2011; *Li et al.*, 2013].
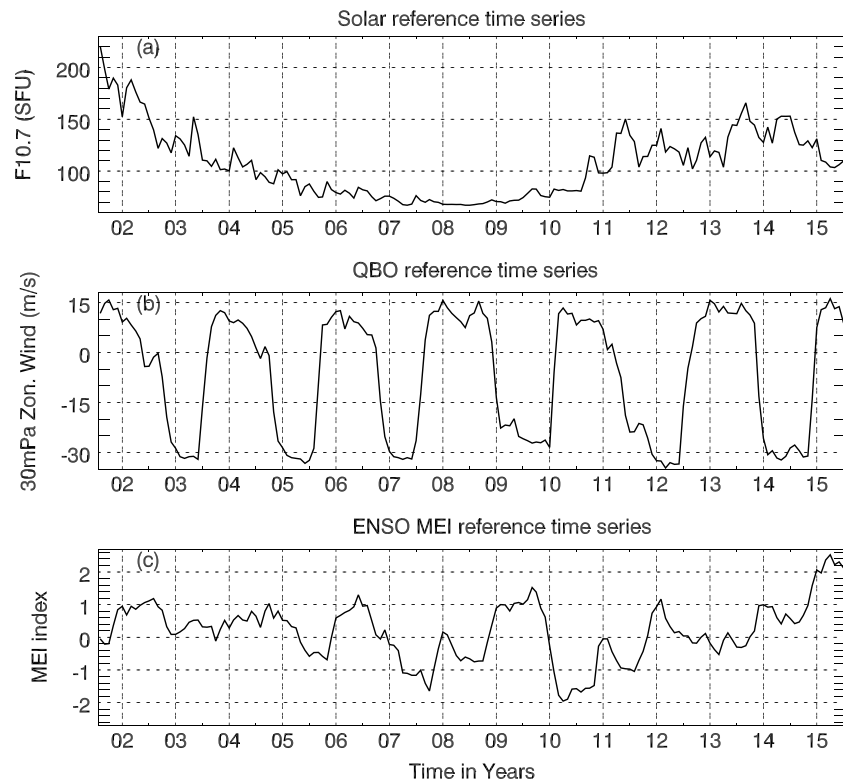
Figure 4. Reference time series used for the regression analyses. (a) Solar radio flux at 10.7 cm ($F_{10.7}$) to characterize the solar cycle, (b) 30 hPa zonal winds over the equator to characterize the QBO, and (c) Multivariate ENSO Index (MEI) to characterize the ENSO signal. The labeled tick marks the 15 June of each year.

3. Global GW Climatology

From Figure 1 we can see that the GW PE in the stratosphere and lower mesosphere (30–70 km) is stronger at high latitudes of the southern winter hemisphere than in the northern winter hemisphere (note that the labeled tick below the *x* axis marks the 15 June of each year). This is consistent with previous observations from different satellite instruments [*Alexander et al.*, 2008; *Ern et al.*, 2011; *X. Liu et al.*, 2014]. In the upper mesosphere and lower thermosphere (80–100 km), the hemispheric asymmetry of GW PE is not as obvious as that in the upper stratosphere or in the lower mesosphere. The latitude distribution of GW PE varies with height [*Ern et al.*, 2011]. At 30–60 km, the GW PE has a prominent peak at higher latitudes and a second peak at around middle latitudes. The second peak occurs during the summer months of each hemisphere and is generated by convectively excited GWs in the subtropics [*Trinh et al.*, 2016]. The second peak shifts to higher latitudes with the increasing altitude. This shift is maintained by the longitudinal structure of gravity wave activity [*Ern et al.*, 2013]. The peak at 70–100 km over low latitudes is likely a bias caused by tides that were not fully removed by the GW extraction method [*Ern et al.*, 2011].

The global GW PE averaged over 14 years (2002–2015), shown in Figure 2a, increases with height from the stratosphere to the mesosphere (from 40 to 95 km). However, the GW PE is nearly constant with height in the lower stratosphere (30–40 km). That is consistent with the pattern of GW derived from GPS/MET (Global Positioning System/Meteorology) but has a smaller magnitude [see *Tsuda et al.*, 2000, Figure 9]. The global RPE, shown in Figure 2b, exhibits semiannual variations from the stratosphere to the mesosphere. The magnitude of RPE is larger in the stratosphere and lower mesosphere (below 70 km) than in the upper mesosphere (above 70 km). From Figure 2b we can see that the amplitude of the semiannual variation of global RPE is relatively stronger during 2006–2010 than that during other years, especially above 75 km. This is consistent with the result documented by *Ern et al.* [2011], who used a 9 year SABER data set and illustrated that GW momentum flux is low in 2002/2003 (higher solar activity) and high in 2008/2009 (lower solar activity) and then lower again after 2009.

It should be noted that the global RPE (Figure 2b) is influenced by its maxima during the summer and winter solstices of each year. Thus, the semiannual variation of global RPE is caused by the two peaks of PRE during the solstices and the two valleys during the equinoxes. Moreover, the larger RPE in July than January is due to the larger RPE in the southern winter than in the northern winter.

The monthly zonal-mean RPE at several latitudes are shown in Figure 3. It can be seen that the temporal variations of the RPE change with height and latitude. At 50°N/S, the annual variation is dominant below 70 km. The annual peak of RPE occurs during the winter months below 70 km and shifts to the summer months above 80 km. At 40°N/S, both annual and semiannual variations exist but the RPE is stronger during the winter months below 70 km and in the summer months above 80 km. The annual variation of RPE below 70 km coincides with the lidar observations in the south of France (44°N), which also showed that the maximum GWs occurring during the winter months [*Wilson et al.*, 1991]. Above 70 km there is a semiannual variation with a larger peak in the summer months and a minor enhancement in the winter months. This is consistent with the seasonal variation of GWs revealed from observations by MU radar, MF radar, lidar, and rocketsondes at middle latitudes [*Manson and Meek*, 1988; *Senft and Gardner*, 1991; *Tsuda et al.*, 1994; *Nakamura et al.*, 1996]. At 30°N/S, the semiannual variation is dominant and the RPE has equivalent magnitude in both winter and summer months. This is consistent with the MF radar observations at Adelaide [*Vincent and Fritts*, 1987]. This is also consistent with the results of *Krebsbach and Preusse* [2007], who used the SABER temperature data between January 2002 and January 2006 and showed similar biennial, annual, and semiannual variations of GWs in the latitude band of 30.0°S ± 2.5° and altitude range of 60.0 ± 1.0 km. At 20°N/S, 10°N/S, and the Equator, the semiannual variation is still dominant but the RPE has a larger magnitude in the summer months than in the winter months below 70 km. This is consistent with the result of *Zhang et al.* [2012], who used the SABER temperature data between January 2002 and December 2009 and showed also the biennial, annual, and semiannual variations of GWs in the latitude band of 10°S–10°N and altitude range of 21–26 km. At 30°S–30°N and above 80 km, the annual and semiannual variations still exist but are not as clear as those below 70 km.

The analyses above illustrate that the relative strengths of annual and semiannual variations are dependent on latitude and height. In general, the annual variation of RPE is prominent at the latitudes higher than 40°N/S and has peak in the winter (summer) months below (above) 70 km. And the semiannual variation of RPE is prominent at the latitudes lower than 30°N/S and has peaks both in the winter and the summer months. The above analyses and comparisons also illustrate that our method of extracting GWs and the global GW climatology is reliable. In the following sections we will study the long-term changes of global GWs and the responses of global GWs to solar activity, QBO, and ENSO.

4. Global Trends of GWs From 2002 to 2015

By applying MLR fit on the time series of RPE from 2002 to 2015, the linear trend (α in equation (1)) of GWs in each month can be obtained as a function of latitude and height (Figure 5). Here we note that there are no long-term trends in the instrument performance or latitude dependent biases that have changed over the 14 years of SABER observations. The confidence level is calculated according to the variance–covariance matrix and the student t test. If the ratio between the fitted long-term trend and its standard deviation is larger than the value of the t distribution at a significance level s, then we claim that the confidence level is $(1 - s) \times 100\%$ for the fitted trend [see *Kutner et al.*, 2004, chapter 2]. The shaded regions shown in Figure 5 indicate the results are not significant at the 90% confidence level. In the following, we focus on the regions with confidence level higher than 90% (i.e., the unshaded regions in Figure 5).

From Figure 5 we can see that there are both positive (red contour lines) and negative (blue contour lines) trends (% per year), which are dependent on month, latitude, and height. The prominent features can be summarized by the following three points: First, a positive trend of 1–2% per year occurs in the height range of 75–90 km and in the latitude band of 30°S–50°S during January and in the latitude band of 30°N–50°N during July. Second, a positive trend of 1–2% per year occurs in the height range of 30–50 km and latitude band of 40°N–50°N during March and in the height range of 40–70 km and latitude band of 30°S–50°S during September. Third, a positive trend of 6–7% per year occurs in the height range of 30–60 km and latitude band of 40°S–50°S during June and in the latitude band of 40°N–50°N during December (with confidence level lower than 90%). The lower confidence level during December might be the result of strong planetary
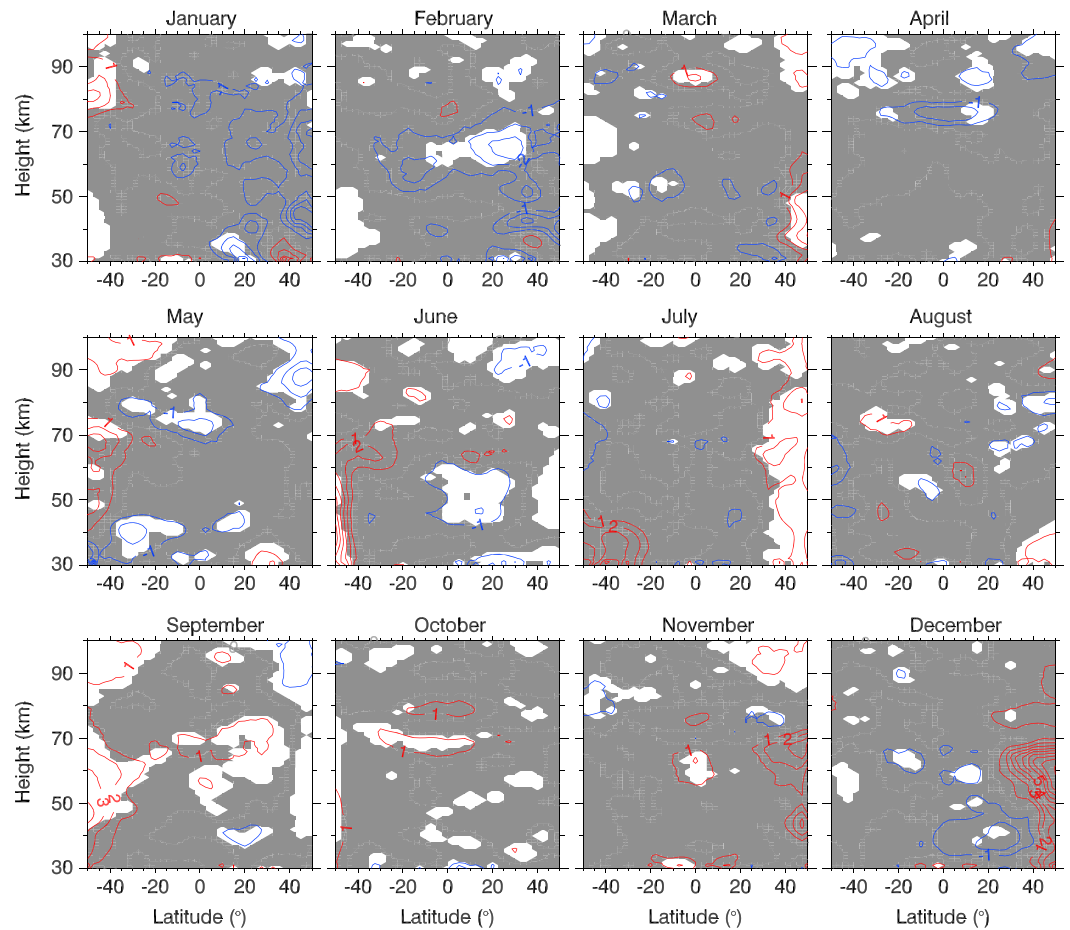
Figure 5. Latitude-height sections of the linear trend term of RPE during each month. The shaded regions indicate where the results are not significant at 90% confidence level. The red and blue contour lines denote positive and negative long-term changes, respectively. The interval of each contour line is 1% RPE per year.

wave activity and sudden stratosphere warmings (SSWs) at northern high latitudes [*Ern et al.*, 2016]. We note that these prominent features are almost symmetric between the two hemispheres since there is a 6 month shift for the atmospheric conditions between the Southern and Northern Hemispheres. Thus, the positive trend of GW RPE in the height range of 75–90 km and latitude band of 30°S–50°S during January is symmetric to that at around 30°N–50°N during July; the positive trend of GW RPE in the height range of 35–50 km and latitude band of 45°N–50°N during March is almost symmetric to that in the latitude band of 45°S–50°S during September; and the positive trend of GW RPE in the height range of 30–60 km and latitude band of 40°S–50°S during June is symmetric to that in the latitude band of 40°N–50°N during December. It should also be noted that the confidence level in the latitude band of 40°S–50°S is larger than 90% during June. The confidence level in the latitude band of 40°N–50°N is lower than 90% during December, which may be due to the strong planetary wave activity and SSWs during the northern winter months [*Ern et al.*, 2016]. Thus, the trends in the latitude band of 40°S–50°S (or at around 50°S) are significant in most months, whereas the trend around 50°N is not significant.

The positive trend of RPE near 50°N during July is qualitatively consistent with the positive trend of GW energy per unit mass (0.6–1.8 m² s⁻² per year) in the height range of 80–88 km derived from 20 years (1990–2010) of MF radar observations at Juliusruh (55°N, 13°E) during July [*Hoffmann et al.*, 2011, Figure 4]. *Hoffmann et al.* [2011] proposed that the positive trend of GWs is due to the selective GW filtering by the changing zonal wind. This is because the zonal wind becomes more westward below 80 km and thereby provides a favorable condition for the eastward propagating GWs, which are dominant in summer months. We note that there is also a positive trend of 1–2% in the height range of 75–90 km and around 50°S during January. This positive trend might also be explained by the selective filtering by the changing zonal wind.
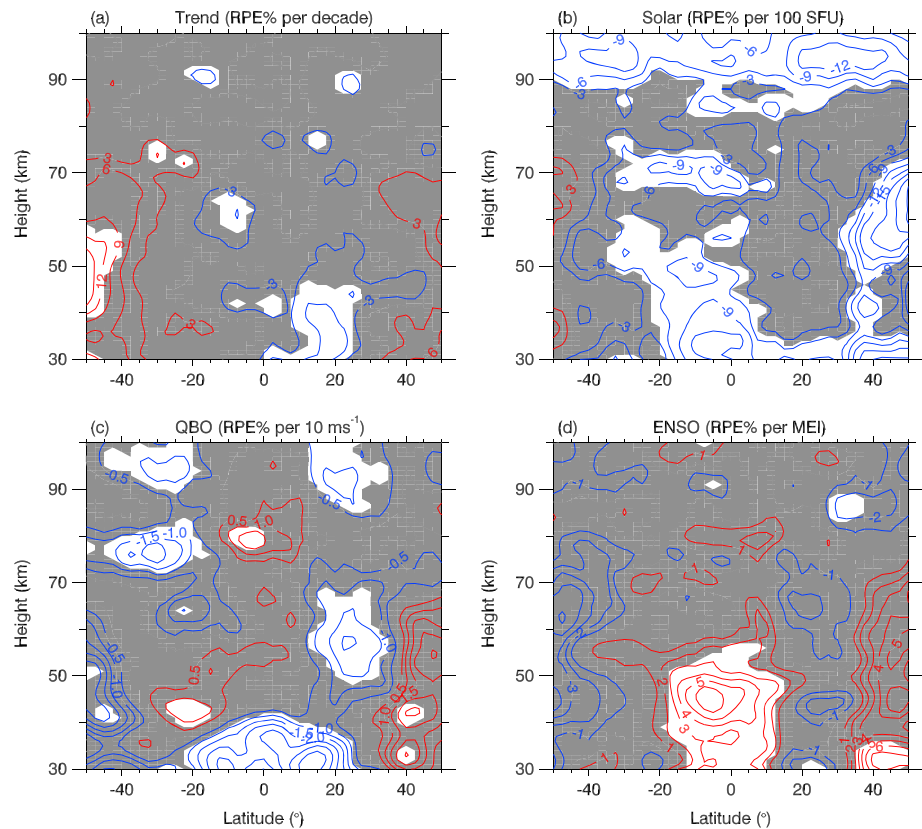
Figure 6. Latitude-height sections of the deseasonalized linear trend term of RPE (a) and the responses of RPE to (b) solar flux, (c) QBO, and (d) ENSO. The shaded regions indicate where the results are not significant at 90% confidence level. The red and blue contour lines denote positive and negative values, respectively. The intervals of each contour line are, respectively, 3% RPE per decade in Figure 6a, 3% RPE per 100 sfu in Figure 6b, 0.5% RPE per 10 m s^{-1} in Figure 6c, and 1% per MEI in Figure 6d.

In the winter months, *Hoffmann et al.* [2011] did not find a clear trend of GW due to the background wind variability. This is also consistent with our results in the winter months (December, January, February), during which there is no significant positive trend in the height range of 75–90 km around 50°N. Moreover, by analyzing the SSW events from 2001 to 2014, *Ern et al.* [2016] provided a comprehensive study on the relations between GW and SSWs and polar-night jet oscillation (PJO) events. They showed that, at northern higher latitudes, SSWs might enhance and/or suppress GW activity, which depends on the particular conditions (e.g., polar vortex split and PJO event). Particularly, the negative trend during January and February might also be influenced by SSWs and PJO events. During these events the GW activity is strongly suppressed [*Ern et al.*, 2016].

The deseasonalized trend of RPE (% per decade) is shown in Figure 6a, which is calculated by MLR fitting on the deseasonalized RPE [*Randel and Cobb*, 1994; *Kutner et al.*, 2004]. From Figure 6a, we can see that there are both positive and negative trends in RPE, depending on the latitude and height. A prominent positive trend at confidence level of 90% occurs in the latitude range of 40°S–50°S and in the height range of 35–60 km. The peak of the positive trend in this region is about 12–15% per decade.

We note that the latitude range of prominent positive trend of RPE is also consistent with the GW's hot spot region in the Southern Hemisphere, where GW RPE is larger than at other latitudes during the southern winter months. These strong GWs are believed to be associated with orography, polar stratospheric night jets, and planetary wave breaking around the polar vortex [*Wu and Eckermann*, 2008; *Preusse et al.*, 2009; *John and Kumar*, 2012; *Hoffmann et al.*, 2013; *X. Liu et al.*, 2014]. Here we can analyze the zonal wind and its trend around the polar vortex to get some possible explanations on the positive trend in GWs. This will be discussed in section 6.

5. Global GW Responses to Solar Activity, QBO Wind, and ENSO

5.1. Responses to Solar Activity

The response of RPE to $F_{10.7}$ is shown in Figure 6b. We can see that in the lower thermosphere (above 90 km), a negative response of RPE to $F_{10.7}$ occurs in the latitude range of 50°S–50°N; in the upper mesosphere and at around the mesopause region (70–90 km), a prominent negative response occurs in the tropical region (25°S–10°N); in the lower mesosphere (50–70 km), there are two regions having negative response (35°S–10°N; 30°N–50°N). In the upper stratosphere (30–50 km), a prominent negative response occurs in the latitude ranges of 30°S–10°N and 30°N–40°N. In general, the responses of RPE to $F_{10.7}$ are negative and exhibit hemispheric asymmetry and are dependent on latitude and height. The strongest response occurs in the latitude band of 30°N–50°N and over a height range of 30–75 km. In contrast there is a wider latitude range of negative response in the Southern Hemisphere.

The negative response of the RPE to $F_{10.7}$ is consistent with the findings of *Ern et al.* [2011], who showed a negative correlation between GW momentum flux and solar flux but used a 9 years SABER data set at 30 km and 70 km. The negative response of RPE to $F_{10.7}$ also coincides with the GW intensity revealed from MF radar observations at Saskatoon (52°N) [*Gavrilov et al.*, 1995]. However, our result does not agree with the result revealed from the radio drift observations at 52°N by *Jacobi et al.* [2006], who found positive correlation between GWs and solar activity. The comparison study based on different instruments at three stations (MU radar at Shigaraki (35°N, 136°E), MF radar at Saskatoon (52°N, 107°W), ionospheric drift velocity measurements at Collm (52°N, 15°E)) by *Gavrilov et al.* [2002] indicated that the correlation between GWs and solar activity is likely dependent on the GW sources (e.g., nonuniform orography in the longitudinal direction) and the conditions of wave propagation at different longitudes. *Gavrilov et al.* [2002] also pointed out that the different measurement methods might also be responsible for the different responses of GW to solar activity. Thus, the response of RPE to $F_{10.7}$ might also be dependent on longitude and will not be discussed here.

5.2. Responses to the QBO

The response of GW RPE to the QBO (as indicated by the 30 hPa zonal wind over the equator) is shown in Figure 6c. From Figure 6c we can see that below 40 km a significant negative response of RPE to the QBO eastward wind phase occurs in the latitude band of 30°S–30°N with more significant response at 0°–30°N than at 0°–30°S. The GW extraction method used here can include some Kelvin waves with shorter periods (either 15 day or 7 day periods) especially near the Equator [*Andrews et al.*, 1987]. Thus, the negative response of RPE to the QBO eastward wind phase could also be related to the fact that eastward propagating Kelvin waves decrease in the eastward wind phase of the QBO. Using SABER temperature data, *Ern et al.* [2008] have shown that Kelvin waves are weak during the eastward wind phase of the QBO (Figure 5a of their paper). The hemispheric asymmetry of the response of RPE to the QBO is consistent with the RPE QBO amplitude and GW PE being larger at 10°N–30°N than at 10°S–30°S, but in the height range of 21–26 km [*Zhang et al.*, 2012]. The hemispherically asymmetric response of RPE to the QBO is also consistent with the fact that the anticorrelation between GW intensity and QBO wind in the latitude band of 15°N–25°N is clearer than in the latitude band of 15°S–25°S [*Ern et al.*, 2011].

There are also two other regions having prominent negative response of RPE to the QBO. One is in the height range of 70–80 km and in the latitude band of 20°S–45°S. The other is in the height range of 50–65 km and latitude band of 15°N–35°N. These two regions seem to originate from the tropical stratosphere and extend to the upper stratosphere in the Northern Hemisphere and to the lower mesosphere in the Southern Hemisphere. Thus, even though the QBO originates in the tropical stratosphere, the influence of the QBO on GW activity can extend to the mesosphere at higher latitudes [*Baldwin et al.*, 2001]. We note that there is positive response of RPE to QBO at around 80 km and the Equator. That is opposite to the negative response in the stratosphere since the QBO phase in the mesosphere is about 180° out of phase with respect to the stratosphere [*Burrage et al.*, 1996; *Mayr et al.*, 1997].

5.3. Responses to ENSO

The response of RPE to ENSO (as indicated by the MEI index) is shown in Figure 6d. From Figure 6d we can see that a significant positive response of RPE to ENSO occurs in the latitude band of 20°S–15°N and from 30 km

to about 55 km. Moreover, there is also a region having positive response in the latitude band of 35°N–50°N and in the height range of below 35 km.

The GW intensity revealed from MF radar observations over Hawaii (22°N, 160°W) is negatively correlated with the Southern Oscillation Index (SOI, a parameter that reflects Pacific ENSO activity) [*Gavrilov et al.*, 2004]. Negative SOI corresponds to El Niño (warm central Pacific), and positive SOI corresponds to La Niña (cool central Pacific) events. Therefore, the negative correlation between SOI and GW intensity implies that GWs are more intense during El Niño conditions. Similarly, the positive response of RPE to MEI shown in Figure 6d means that strong El Niño (large positive MEI index) corresponds to strong GW intensity. Thus, the positive response of RPE to ENSO in the tropical stratosphere found here is consistent with the result of *Gavrilov et al.* [2004]. A possible mechanism is that El Niño events may strengthen convective GW sources in the tropical region and change the atmospheric wind and temperature structure [*Geller et al.*, 2016; *Sato et al.*, 2016].

6. Discussion

Recent studies showed that the rapidly increasing CO_2 in the mesosphere and lower thermosphere regions reported by *Yue et al.* [2015] could be reproduced by increasing eddy diffusion coefficient by 15% per decade in a 1-D model [*Emmert et al.*, 2012] and 30% per decade in WACCM [*Garcia et al.*, 2016]. Although the monthly or deseasonalized trend of GWs estimated here is not positive throughout the year and globally, there exist positive GW trends in some months and at some latitudes. Moreover, the positive trend of GWs has a peak of about 12–15% per decade at around 50°S, which can provide some observational evidence that the eddy diffusion coefficient is increasing in some places. However, these significant positive trends of GWs occur below 80 km and cannot explain the rapidly increasing CO_2 in the mesosphere and lower thermosphere. We note that the SABER observations cannot capture all GWs (from lowest- to highest-frequency GWs or from shortest to longest wavelength GWs) but can capture only GWs with horizontal wavelengths longer than about 100–200 km or vertical wavelengths longer than 4 km [*Preusse et al.*, 2002, 2009]. Thus, the SABER instrument cannot resolve GWs with horizontal wavelengths shorter than 100 km and/or vertical wavelengths shorter than 4 km. These GWs with shorter horizontal wavelengths can contribute greatly to the eddy diffusion but are overlooked by SABER observation due to the limitation of limb sounding.

Now we discuss the possible mechanisms for the trends of GW RPE since it has significant latitude and seasonal dependence. The trend of GW RPE shown in Figures 5 and 6a is positive and is significant at around 50°S, which is also the latitude band of the polar stratospheric jet. On the other hand, the trends of GW RPE shown in Figure 5 can be summarized as showing positive trends of RPE during the Southern Hemispheric (SH) spring equinox (September at around 50°S) and during the SH winter solstices (June at around 50°S, 60°S).

It is generally accepted that the GWs in the stratosphere and mesosphere are related to the GW sources (orography, convection, jet/front systems, and planetary wave breaking) and propagation conditions (background winds and atmospheric stabilities) [*Nappo*, 2002; *Fritts and Alexander*, 2003; *Hertzog et al.*, 2008; *Jiang et al.*, 2005, 2006; *John and Kumar*, 2012; *X. Liu et al.*, 2014; *Plougonven and Zhang*, 2014; *Thurairajah et al.*, 2014; *Ern et al.*, 2016]. At the southern higher latitudes, the GWs generated by orography are comparable to the nonorographic GWs on zonal average, as revealed by *Hertzog et al.* [2008] from balloon observations and by *Plougonven et al.* [2013] through mesoscale Weather Research and Forecast model simulations. Since the positive trends of RPE occur only in the latitude band where the polar tropopause jet and the polar stratospheric jet occur, which are important for GW generation and propagation, we will analyze the polar tropospheric and stratospheric wind and its trend to find possible relations between the trends of GWs and the polar stratospheric wind.

The MERRA (Modern Era Retrospective-analysis for Research and Applications) [*Rienecker et al.*, 2011] zonal-mean zonal wind is used to explore the possible relations between the trend of GWs and the polar tropospheric and stratospheric wind. The zonal-mean zonal winds in the latitude bands of 45°N–55°N (with center at 50°N) and 45°S–55°S (with center at 50°S) are averaged to represent the polar tropospheric and stratospheric wind. Then the polar winds from 2002 to 2015 are binned into months to construct seasonal cycles, as shown in Figures 7a and 7b. Moreover, the trends of polar stratospheric winds in each month for the period 2002–2015 are shown in Figures 7c and 7d. For convenience, we also show the long-term changes of RPE at
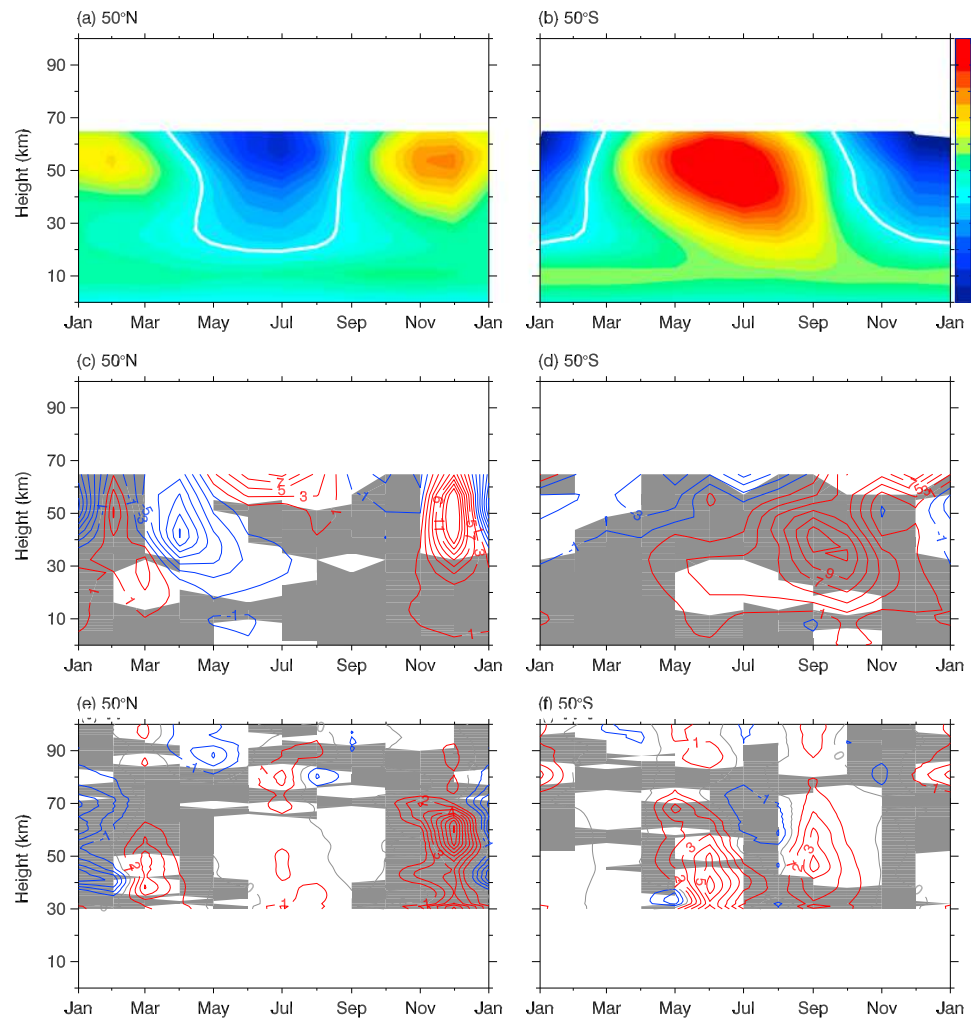
Figure 7. Month-height sections of the MERRA zonal-mean zonal winds at (a) 50°N and (b) 50°S in a binned year, which is calculated by binning the winds from 2002 to 2015 into 1 year. The white contour lines shown in Figures 7a and 7b are zero wind lines. The unit of color bar for Figures 7a and 7b is m s^{-1}. The linear trend terms of zonal-mean zonal winds at (c) 50°N and (d) 50°S in each month for the period of 2002–2015. The long-term changes of GW PE at (e) 50°N and (f) 50°S in each month for the period of 2002–2015. The shaded regions indicate that the results are not significant at 90% confidence level. The red and blue contour lines denote positive and negative values, respectively. The intervals of each contour line are 2 m s^{-1} per decade in Figures 7c and 7d and 1% RPE per year in Figures 7e and 7f.

50°N and 50°S in each month for the period 2002–2015 in Figures 7e and 7f, which are subsets of the data in Figure 5.

From Figures 7a and 7c we can see that the zonal-mean zonal wind is eastward during December at 50°N. The positive trend of zonal wind in the height range of 20–60 km during December indicates that the polar stratospheric jet became more eastward near 50°N over the past 14 years. This supports the slightly positive trend of GWs at around 50°N and 30–70 km during December shown in Figures 5, 6a, and 7e. This is likely because the polar stratospheric jet and the associated polar vortex is one of the main sources of GWs [*Gavrilov and Fukao*, 1999; *Yoshiki and Sato*, 2000; *Yamashita et al.*, 2009]. The fast eastward zonal wind and the associated positive trend provide favorable conditions for westward propagating GWs during December. The presence of westward propagating GWs is supported by radiosonde observations over the Arctic, which also showed that GWs propagate against the mean eastward wind [*Yoshiki and Sato*, 2000]. Figure 7c shows that there is a significant negative trend during March and April at 50°N. However, a significant negative trend of GW RPE does not occur during March or April at 50°N (Figure 7e). Comparing with the zonal-mean wind shown in Figure 7a, a possible explanation is that the weak eastward wind (near the zero wind) during March and

April cannot generate much GWs. As for the GW propagation condition, the wind reversal during March and April might also filter out some GWs with zero and/or slow horizontal phase speed, such as orography-generated GWs and jet-generated GWs [*Plougonven and Zhang*, 2014].

To explain the positive trends of GWs at around 50°S, we consider wave sources (the polar stratospheric jet-generated GWs and tropopause jet-generated GWs) and GW propagation conditions. First, we examine the polar stratospheric jet-generated GWs and their propagation conditions. From Figure 7b we can see that the zonal-mean zonal wind at 50°S is eastward from March to October with peak during June at the stratopause. The significant positive trend of zonal-mean zonal wind shown in Figure 7d occurs from September to November with peak during October and in the height range of 20–60 km. This positive trend in the zonal-mean zonal wind is consistent qualitatively with the results of *Sun et al.* [2014], who used the Interim European Centre for Medium-Range Weather Forecasts Re-Analysis (ERA-Interim) data from 1980 to 2001 in the latitude band of 50°S–70°S. In addition, using the National Center for Environmental Prediction-National Center for Atmospheric Research data from 1959 to 2002, *Kanukhina et al.* [2008] showed that the zonal-mean zonal wind is accelerated in the higher middle latitudes of the troposphere and lower stratosphere on average. For the new released MERRA2 data, Figure 15 of *Molod et al.* [2015] showed that the patterns of mean wind are similar to Figure 7b but the zero wind line is higher in altitude and is delayed in time in MERRA2 compared to MERRA. Since the polar stratospheric jet is a source of GWs [*Gavrilov and Fukao*, 1999; *Yoshiki and Sato*, 2000; *Hertzog et al.*, 2008; *Yamashita et al.*, 2009; *Ern et al.*, 2016], the eastward zonal wind and the associated positive trend of zonal wind might indicate that the jet-generated GWs increase from 2002 to 2015. The statistical study by *Yoshiki and Sato* [2000] showed that the propagating direction of GWs varied with locations and the GW energy is highly correlated with the stratospheric wind. This indicated that the polar stratospheric night jet might be a source of GWs in Antarctica. The zonal-mean zonal wind in Figure 7b changes its direction in the upper stratosphere from eastward during September to westward during November. Consequently, the jet-generated GWs propagate eastward with height in a reduced background wind or even in a reversed background wind. This ensures faster intrinsic phase speeds and larger GW amplitudes in the upper stratosphere [*Smith et al.*, 1987; *Liu and Xu*, 2007; *Ern et al.*, 2015]. This supports the positive trend of GWs during September and October at around 50°S shown in Figures 5 and 6a. It should be noted that the trend of GWs is significantly lower than 50°S but could not be calculated at latitudes higher than 50°S during October due to the sampling pattern of SABER.

Second, we examine the tropopause jet-generated GWs and their propagation conditions. Figure 7d shows that the zonal-mean zonal wind has a positive trend below 20 km at around 50°S from April to December. This indicates that GW source processes related to the strength of the tropopause jet may act more strongly, thus explaining the observed increase in GW PE. Consequently, the strengthening tropopause winds might be the dominant effect and be responsible for the positive trend of GW RPE over a larger altitude range.

A short summary of the above three points is that the increasing polar stratospheric jet supports the positive trend of GWs in the lower mesosphere. The increasing tropopause jet supports the positive trend of GWs in the stratosphere.

Comparison on the zonal-mean zonal winds (Figures 7a and 7b) shows that the stratospheric zonal wind is stronger at 50°S than that at 50°N during the winter months of each hemisphere. Thus, GWs are stronger in the southern polar region than that in the northern polar region [*John and Kumar*, 2012; *Zhang et al.*, 2012; *X. Liu et al.*, 2014]. Moreover, comparison on the trends in the MERRA zonal winds (Figures 7c and 7d) shows that the significant positive trends at 50°S are larger and longer lasting than that at 50°N. This supports the significant positive trend of GW RPE in the latitudes around 50°S shown in Figures 5 and 6a.

It should be noted that further discussions on the responses of GWs to solar activity, QBO, and ENSO are also important to elucidate the mechanisms influencing the GWs in the middle and upper atmosphere. Numerical simulation based on GCMs might be a good choice to elucidate the mechanisms. This is not done in this work and will be studied in our future work.

7. Summary and Conclusions

We analyzed the global GW activity derived from SABER temperature profiles over the past 14 years (2002–2015). Since the data covered longer than a solar cycle, we studied the linear trend of GW and the responses

of GW to solar activity, QBO, and ENSO. Possible mechanisms of inducing the trend of GW are discussed using the MERRA wind data during the same period as SABER observations.

Over the past 14 years, GWs are stronger in the high latitudes of the southern winter hemisphere than those in the northern winter hemisphere. Comparing with the northern winter hemisphere, the stronger- and longer-lasting polar stratospheric jet might be responsible for the stronger GWs in the southern winter hemisphere. The relative strengths of annual and semiannual variations are dependent on latitude and height. Specifically, the annual variation of GW PE is prominent at the latitudes higher than 40°N/S and has peaks during the winter (summer) months below (above) 70 km. And the semiannual variation of GW PE is prominent at the latitudes lower than 30°N/S and has peaks both during the winter and the summer months.

The trend of GWs depends on month, latitude, and height. The significant positive trend of GWs at around 50°N during July is consistent with that derived from MF radar observations in the height range of 80–88 km. The significant positive trends of GWs are mostly at the latitudes around 50°S, the latitude of polar stratospheric jet maximum. Since the polar stratospheric jet is an important source of GWs in the polar region, the positive trends of polar stratospheric jet derived from MERRA wind data support the significant positive trend of GWs at around 50°S.

Both the monthly and the deseasonalized trends of GWs are significant at around 50°S. By analyzing the zonal-mean zonal wind and its trends derived from MERRA data, we found that the zonal-mean zonal wind has positive trend with peak at the stratopause region. According to previous studies, the propagating direction of GWs is against the eastward zonal-mean zonal wind and there are correlations between GWs and stratospheric wind over Antarctica, we speculate that the increasing polar stratospheric jet supports the positive trend of GWs in the upper stratosphere and lower mesosphere. The increasing tropopause jet supports the positive trend of GWs in the stratosphere.

We should note that the analysis does not show that long-term trends of GWs are responsible for eddy diffusion changes needed to account for large CO_2 trends; however, GWs with wavelengths to which SABER is not sensitive might still be responsible.

The responses of global GWs to solar activity, QBO, and ENSO are also analyzed. The global GWs response to $F_{10.7}$ is negative in the lower and middle latitudes, especially in the upper mesosphere and the lower thermosphere. The response of global GWs to the QBO eastward wind phase is negative in the tropical upper stratosphere and extend to higher latitudes at a higher altitude. The response of global GWs to the QBO eastward wind phase is more negative in the tropical region of Northern Hemisphere than that of Southern Hemisphere. The response of global GWs to the ENSO MEI index is positive in the tropical stratosphere.

Appendix A: Method of Extracting GW

The GW extraction method used here is similar to that proposed by *Fetzer and Gille* [1994], *Preusse et al.* [2002, 2009], *Yamashita et al.* [2013], and *X. Liu et al.* [2014]. The detailed procedure for extracting GW from SABER temperature profiles can be described by the following five steps. The SABER temperature data in the ascending node at 22 June 2015 (summer solstice) and around 45°S are taken as an example to illustrate the method.

First, the daily SABER temperature profiles ($T(z)$) in a latitude band of 5° are rearranged in increasing order with increasing longitude to produce a longitude-height distribution of temperature (shown in Figure A1a). This rearrangement is performed in the ascending and descending nodes, respectively, such that it minimizes the influences of tides on GWs [*Preusse et al.*, 2009; *Yamashita et al.*, 2013]. For the data shown Figure A1a, their mean local time (LT) is 23.2 h with a standard deviation of 0.24 h. The mean latitude is 45.27°S with a standard deviation of 1.53°. The nearly identical LT can also minimize the influences of tides on GWs.

Second, the longitude-height distribution of temperature at each height is fitted by least square (LS) harmonic fitting [*Lomb*, 1976] with zonal wave numbers from 0 to 7 [*Preusse et al.*, 2009; *Yamashita et al.*, 2013; *X. Liu et al.*, 2014; *Thurairajah et al.*, 2014] to get the background temperature ($T_0(z)$) (Figure A1b), such that tides and planetary waves can be eliminated efficiently since they have longer horizontal wavelengths.

Third, the perturbation temperature $T'(z)$ is calculated by removing the background temperature from the observed temperature, $T'(z) = T(z) - T_0(z)$ (black line in Figure A1c).
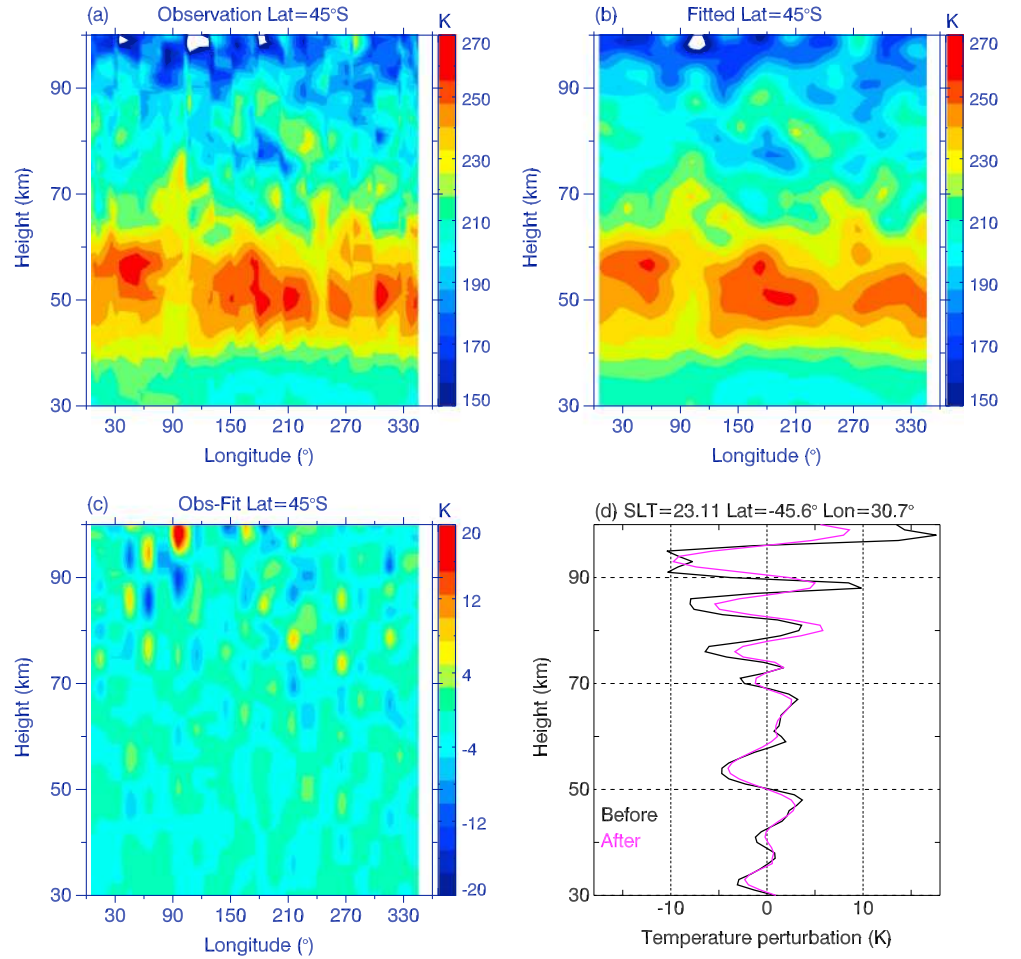
Figure A1. Flow chart of extracting GW profiles. (a) The observed temperature at 45°S and ascending node of 22 June 2015, (b) the fitted temperature obtained by LS fitting with zonal wave numbers 0–7, (c) the perturbation temperature obtained by subtracting the fitted temperature from the observed temperature, and (d) the perturbation temperature (black) and the reconstructed GW profiles by wavelet analysis (magenta).

Fourth, we perform wavelet analysis [*Torrence and Compo*, 1998] on each perturbation temperature profile $T'(z)$ and get three dominant vertical wavelengths in the range of 4–30 km. Then the three dominant vertical wavelengths are selected to reconstruct a new perturbation temperature profile ($T''(z)$ (magenta line Figure A1d), which is used to calculate the GW potential energy (PE) per unit mass [*Preusse et al.*, 2009; *Yamashita et al.*, 2013]. The GW PE per unit mass of each observed temperature profile is given by [*Tsuda et al.*, 2000; *Wang and Geller*, 2003; *X. Liu et al.*, 2014; *Thurairajah et al.*, 2014]

$$E_p(z) = \frac{1}{2}\left(\frac{g}{N(z)}\right)^2\left(\frac{T''(z)}{T_0(z)}\right)^2,$$

(A1)

where g is the gravitational acceleration. The Brunt-Väisälä frequency $N(z)$ in equation (A1) is calculated by

$$N(z) = \left[\left(\frac{g}{T_0(z)}\right)\left(\frac{g}{c_p} + \frac{\partial T_0(z)}{\partial z}\right)\right]^{1/2}.$$

(A2)

Here $c_p = 1004.5$ J kg^{-1} K^{-1} is the specific heat of dry air at constant pressure.

Finally, the GW PE of all the observed temperature profiles in each day is binned into 20° × 5° (longitude times latitude) in horizontal boxes and 1 km in vertical grid. The horizontal boxes have overlap of 10° in longitude and 2.5° in latitude, respectively. Thus, there are 36 grids in longitude from 5° to 355° and 45 grids in latitude from 50°S to 50°N.

References

Alexander, M. J. (2015), Global and seasonal variations in three-dimensional gravity wave momentum flux from satellite limb-sounding temperatures, *Geophys. Res. Lett.*, *42*, 6860–6867, doi:10.1002/2015GL065234.

Alexander, M. J., and C. Barnet (2007), Using satellite observations to constrain parameterizations of gravity wave effects for global models, *J. Atmos. Sci.*, *64*, 1652–1665.

Alexander, M. J., et al. (2008), Global estimates of gravity wave momentum flux from high resolution dynamics limb sounder observations, *J. Geophys. Res.*, *113*, D15S18, doi:10.1029/2007JD008807.

Alexander, M. J., et al. (2010), Recent developments in gravity-wave effects in climate models and the global distribution of gravity-wave momentum flux from observations and models, *Q. J. R. Meteorol. Soc.*, *136*, 1103–1124.

Andrews, D. G., J. R. Holton, and C. B. Leovy (1987), *Middle Atmosphere Dynamics*, pp. 202–215, Academic Press, San Diego, Calif.

Baldwin, M. P., et al. (2001), The quasi-biennial oscillation, *Rev. Geophys.*, *39*, 179–229, doi:10.1029/1999RG000073.

Burrage, M. D., R. A. Vincent, H. G. Mayr, W. R. Skinner, N. F. Arnold, and P. B. Hays (1996), Long-term variability of the equatorial middle atmosphere zonal wind, *J. Geophys. Res.*, *101*, 12,847–12,854, doi:10.1029/96JD00575.

Emmert, J. T., M. H. Stevens, P. F. Bernath, D. P. Drob, and C. D. Boone (2012), Observations of increasing carbon dioxide concentration in Earth's thermosphere, *Nat. Geosci.*, *5*, 868–871, doi:10.1038/NGEO1626.

Ern, M., P. Preusse, M. J. Alexander, and C. D. Warner (2004), Absolute values of gravity wave momentum flux derived from satellite data, *J. Geophys. Res.*, *109*, D20103, doi:10.1029/2004JD004752.

Ern, M., P. Preusse, M. Krebsbach, M. G. Mlynczak, and J. M. Russell III (2008), Equatorial wave analysis from SABER and ECMWF temperatures, *Atmos. Chem. Phys.*, *8*, 845–869, doi:10.5194/acp-8-845-2008.

Ern, M., P. Preusse, J. C. Gille, C. L. Hepplewhite, M. G. Mlynczak, J. M. Russell III, and M. Riese (2011), Implications for atmospheric dynamics derived from global observations of gravity wave momentum flux in stratosphere and mesosphere, *J. Geophys. Res.*, *116*, D19107, doi:10.1029/2011JD015821.

Ern, M., P. Preusse, S. Kalisch, M. Kaufmann, and M. Riese (2013), Role of gravity waves in the forcing of quasi two-day waves in the mesosphere: An observational study, *J. Geophys. Res. Atmos.*, *118*, 3467–3485, doi:10.1029/2012JD018208.

Ern, M., F. Ploeger, P. Preusse, J. C. Gille, L. J. Gray, S. Kalisch, M. G. Mlynczak, J. M. Russell III, and M. Riese (2014), Interaction of gravity waves with the QBO: A satellite perspective, *J. Geophys. Res. Atmos.*, *119*, 2329–2355, doi:10.1002/2013JD020731.

Ern, M., P. Preusse, and M. Riese (2015), Driving of the SAO by gravity waves as observed from satellite, *Ann. Geophys.*, *33*, 483–504, doi:10.5194/angeo-33-483-2015.

Ern, M., et al. (2016), Satellite observations of middle atmosphere gravity wave absolute momentum flux and of its vertical gradient during recent stratospheric warmings, *Atmos. Chem. Phys.*, *16*, 9983–10,019, doi:10.5194/acp-16-9983-2016.

Fetzer, E. J., and J. C. Gille (1994), Gravity wave variances in LIMS temperatures. Part I. Variability and comparison with background winds, *J. Atmos. Sci.*, *51*, 2461–2483.

Fritts, D. C., and M. J. Alexander (2003), Gravity wave dynamics and effects in the middle atmosphere, *Rev. Geophys.*, *41*(1), 1003, doi:10.1029/2001RG000106.

Garcia, R. R., M. López-Puertas, B. Funker, D. E. Kinnison, D. R. Marsh, and L. Qian (2016), On the secular trend of CO_x and CO_2 in the lower thermosphere, *J. Geophys. Res. Atmos.*, *121*, 3634–3644, doi:10.1002/2015JD024553.

Gavrilov, N. M., A. H. Manson, and C. E. Meek (1995), Climatological monthly characteristics of middle atmosphere gravity waves (10 min-10 h) during 1979–1993 at Saskatoon, *Ann. Geophys.*, *13*, 285–295.

Gavrilov, N. M., and S. Fukao (1999), A comparison of seasonal variations of gravity wave intensity observed by MU radar with a theoretical model, *J. Atmos. Sci.*, *56*(20), 3485–3494.

Gavrilov, N. M., S. Fukao, T. Nakamura, C. Jacobi, D. Kürschner, A. H. Manson, and C. E. Meek (2002), Comparative study of interannual changes of the mean winds and gravity wave activity in the middle atmosphere over Japan, Central Europe and Canada, *J. Atmos. Sol. Terr. Phys.*, *64*, 1003–1010.

Gavrilov, N. M., D. M. Riggin, and D. C. Fritts (2004), Interannual variations of the mean wind and gravity wave variances in the middle atmosphere over Hawaii, *J. Atmos. Sol. Terr. Phys.*, *66*, 637–645, doi:10.1016/j.jastp.2004.01.015.

Geller, M. A., T. Zhou, and W. Yuan (2016), The QBO, gravity waves forced by tropical convection, and ENSO, *J. Geophys. Res. Atmos.*, *121*, 8886–8895, doi:10.1002/2015JD024125.

Gong, J., J. Yue, and D. L. Wu (2015), Global survey of concentric gravity waves in AIRS images and ECMWF analysis, *J. Geophys. Res. Atmos.*, *120*, 2210–2228, doi:10.1002/2014JD022527.

Hertzog, A., G. Boccara, R. A. Vincent, F. Vial, and P. Cocquerez (2008), Estimation of gravity-wave momentum flux and phase speeds from quasi-Lagrangian stratospheric balloon flights: 2. Results from the Vorcore campaign in Antarctica, *J. Atmos. Sci.*, *65*, 3056–3070.

Hoffmann, P., M. Rapp, W. Singer, and D. Keuer (2011), Trends of mesospheric gravity waves at northern middle latitudes during summer, *J. Geophys. Res.*, *116*, D00P08, doi:10.1029/2011JD015717.

Hoffmann, L., X. Xue, and M. J. Alexander (2013), A global view of stratospheric gravity wave hotspots located with Atmospheric Infrared Sounder observations, *J. Geophys. Res. Atmos.*, *118*, 416–434, doi:10.1029/2012JD018658.

Holt, L. A., M. J. Alexander, L. Coy, A. Molod, W. Putman, and S. Pawson (2016), Tropical waves and the quasi-biennial oscillation in a 7-km global climate simulation, *J. Atmos. Sci.*, *73*, 3771–3783, doi:10.1175/JAS-D-15-0350.1.

Holton, J. R. (1983), The influence of gravity wave breaking on the general circulation of the middle atmosphere, *J. Atmos. Sci.*, *40*, 2497–2507.

Jacobi, C., N. M. Gavrilov, D. Kürschner, and K. Fröhlich (2006), Gravity wave climatology and trends in the mesosphere/lower thermosphere region deduced from low-frequency drift measurements 1984–2003 (52.1°N, 13.2°E), *J. Atmos. Sol. Terr. Phys.*, *68*, 1913–1923, doi:10.1016/j.jastp.2005.12.007.

Jiang, J. H., S. D. Eckermann, D. L. Wu, K. Hocke, B. Wang, J. Ma, and Y. Zhang (2005), Seasonal variation of gravity wave sources from satellite observation, *Adv. Space Res.*, *35*, 1925–1932.

Jiang, J. H., D. L. Wu, and D.-Y. Wang (2006), Interannual variation of gravity waves in the Arctic and Antarctic winter middle atmosphere, *Adv. Space Res.*, *38*, 2418–2423.

John, S. R., and K. K. Kumar (2012), TIMED/SABER observations of global gravity wave climatology and their interannual variability from stratosphere to mesosphere lower thermosphere, *Clim. Dyn.*, doi:10.1007/s00382-012-1329-9.

Kanukhina, A. Y., E. V. Suvorova, L. A. Nechaeva, E. K. Skrygina, and A. I. Pogoreltsev (2008), Climatic variability of the mean flow and stationary planetary waves in the NCEP/NCAR reanalysis data, *Ann. Geophys.*, *26*, 1233–1241.

Kim, Y., S. D. Eckermann, and H. Chun (2003), An overview of the past, present and future of gravity-wave drag parametrization for numerical climate and weather prediction models, *Atmos. Ocean*, *41*(1), 65–98, doi:10.3137/ao.410105.

Krebsbach, M., and P. Preusse (2007), Spectral analysis of gravity wave activity in SABER temperature data, *Geophys. Res. Lett.*, *34*, L03814, doi:10.1029/2006GL028040.

Kutner, M. H., C. J. Nachtsheim, J. Neter, and W. Li (2004), *Applied Linear Statistical Models*, 5th ed., pp. 40–88 and pp. 214–247, Mcgraw-Hill/Irwin, San Francisco, Calif.

Li, T., T. Leblanc, I. S. McDermid, D. L. Wu, X. Dou, and S. Wang (2010), Seasonal and interannual variability of gravity wave activity revealed by long-term lidar observations over Mauna Loa Observatory, Hawaii, *J. Geophys. Res.*, *115*, D13103, doi:10.1029/2009JD013586.

Li, T., N. Calvo, J. Yue, X. Dou, J. M. Russell III, M. G. Mlynczak, C.-Y. She, and X. Xue (2013), Influence of El Niño-Southern Oscillation in the mesosphere, *Geophys. Res. Lett.*, *40*, 3292–3296, doi:10.1002/grl.50598.

Lindzen, R. S. (1981), Turbulence and stress due to gravity waves and tidal breakdown, *J. Geophys. Res.*, *86*, 9707–9714, doi:10.1029/JC086iC10p09707.

Liu, H.-L., P. B. Hays, and R. G. Roble (1999), A numerical study of gravity wave breaking and impacts on turbulence and mean state, *J. Atmos. Sci.*, *56*(13), 2152–2177.

Liu, H.-L., J. M. McInerney, S. Santos, P. H. Lauritzen, M. A. Taylor, and N. M. Pedatella (2014), Gravity waves simulated by high-resolution Whole Atmosphere Community Climate Model, *Geophys. Res. Lett.*, *41*, 9106–9112, doi:10.1002/2014GL062468.

Liu, X., and J. Xu (2007), Nonlinear interaction between gravity wave and different mean wind, *Prog. Nat. Sci.*, *17*(6), 639–644.

Liu, X., J. Yue, J. Xu, L. Wang, W. Yuan, J. M. Russell III, and M. E. Hervig (2014), Gravity wave variations in the polar stratosphere and mesosphere from SOFIE/AIM temperature observations, *J. Geophys. Res. Atmos.*, *119*, 7368–7381, doi:10.1002/2013JD021439.

Lomb, N. R. (1976), Least-square frequency analysis of unequally spaced data, *Astrophys. Space Sci.*, *39*, 447–462.

Manson, A. H., and C. E. Meek (1988), Gravity wave propagation characteristics (60–120 km) as determined by the Saskatoon MF radar (Gravnet) system: 1983–85 at 52N, 107W, *J. Atmos. Sci.*, *45*, 932–946.

Mayr, H. G., J. G. Mengel, C. O. Hines, K. L. Chan, N. F. Arnold, C. A. Reddy, and H. S. Porter (1997), The gravity wave Doppler spread theory applied in a numerical spectral model of the middle atmosphere. 2. Equatorial oscillations, *J. Geophys. Res.*, *102*, 26,093–26,105, doi:10.1029/96JD03214.

Molod, A., L. Takacs, M. Suarez, and J. Bacmeister (2015), Development of the GEOS-5 atmospheric general circulation model: Evolution from MERRA to MERRA2, *Geosci. Model Dev.*, *8*, 1339–1356, doi:10.5194/gmd-8-1339-2015.

Nakamura, T., T. Tsuda, S. Fukao, A. H. Manson, C. E. Meek, R. A. Vincent, and I. M. Reid (1996), Mesospheric gravity waves at Saskatoon (52°N), Kyoto (35°N), and Adelaide (35°S), *J. Geophys. Res.*, *101*, 7005–7012, doi:10.1029/95JD03826.

Nappo, C. J. (2002), *An Introduction to Atmospheric Gravity Waves*, pp. 47–84, Academic Press, San Diego, Calif.

Plougonven, R., A. Hertzog, and L. Guez (2013), Gravity waves over Antarctica and the Southern Ocean: Consistent momentum fluxes in mesoscale simulations and stratospheric balloon observations, *Q. J. R. Meteorol. Soc.*, *139*, 101–118.

Plougonven, R., and F. Zhang (2014), Internal gravity waves from atmospheric jets and fronts, *Rev. Geophys.*, *52*, 33–76, doi:10.1002/2012RG000419.

Preusse, P., A. Dörnbrack, S. D. Eckermann, M. Riese, B. Schaeler, J. Bacmeister, D. Broutman, and K. U. Grossmann (2002), Space based measurements of stratospheric mountain waves by CRISTA: 1. Sensitivity, analysis method and a case study, *J. Geophys. Res.*, *107*(D23), 8178, doi:10.1029/2001JD000699.

Preusse, P., et al. (2006), Tropopause to mesopause gravity waves in August: Measurement and modeling, *J. Atmos. Sol. Terr. Phys.*, *68*(15), 1730–1751, doi:10.1016/j.jastp.2005.10.019.

Preusse, P., S. D. Eckermann, M. Ern, J. Oberheide, R. H. Picard, R. G. Roble, M. Riese, J. M. Russell III, and M. G. Mlynczak (2009), Global ray tracing simulations of the SABER gravity wave climatology, *J. Geophys. Res.*, *114*, D08126, doi:10.1029/2008JD011214.

Randel, W. J., and J. B. Cobb (1994), Coherent variations of monthly mean total ozone and lower stratospheric temperature, *J. Geophys. Res.*, *99*, 5433–5447, doi:10.1029/93JD03454.

Randel, W. J., R. R. Garcia, N. Calvo, and D. Marsh (2009), ENSO influence on zonal mean temperature and ozone in the tropical lower stratosphere, *Geophys. Res. Lett.*, *36*, L15822, doi:10.1029/2009GL039343.

Remsberg, E. E., et al. (2008), Assessment of the quality of the version 1.07 temperature-versus-pressure profiles of the middle atmosphere from TIMED/SABER, *J. Geophys. Res.*, *113*, D17101, doi:10.1029/2008JD010013.

Rienecker, M. M., et al. (2011), MERRA: NASA's modern-era retrospective analysis for research and applications, *J. Clim.*, *24*, 3624–3648, doi:10.1175/JCLI-D-11-00015.1.

Roble, R. G. (1995), Energetics of the mesosphere and thermosphere, in *The Upper Mesosphere and Lower Thermosphere: A Review of Experiment and Theory*, Geophys. Monogr. Ser., vol. 87, edited by R. M. Johnson and T. L. Killeen, pp. 1–21, AGU, Washington, D. C., doi:10.1029/GM087p0001.

Russell, J. M., III, M. G. Mlynczak, L. L. Gordley, J. Tansock, and R. Esplin (1999), An overview of the SABER experiment and preliminary calibration results, *Proc. SPIE*, *3756*, 277–288.

Sato, K., C. Tsuchiya, M. J. Alexander, and L. Hoffmann (2016), Climatology and ENSO-related interannual variability of gravity waves in the Southern Hemisphere subtropical stratosphere revealed by high-resolution AIRS observations, *J. Geophys. Res. Atmos.*, *121*, 7622–7640, doi:10.1002/2015JD024462.

Senft, D. C., and C. S. Gardner (1991), Seasonal variability of gravity wave activity and spectra in the mesopause region at Urbana, *J. Geophys. Res.*, *96*, 17,229–17,264, doi:10.1029/91JD01662.

Smith, S. A., D. C. Fritts, and T. E. Van Zandt (1987), Evidence of a saturation spectrum of atmospheric gravity waves, *J. Atmos. Sci.*, *44*, 1404–1410.

Sun, L., G. Chen, and W. A. Robinson (2014), The role of stratospheric polar vortex breakdown in Southern Hemisphere climate trends, *J. Atmos. Sci.*, *71*, 2335–2353.

Tapping, K. F. (2013), The 10.7 cm solar radio flux ($F_{10.7}$), *Space Weather*, *11*, 394–406, doi:10.1002/swe.20064.

Thurairajah, B., S. M. Bailey, C. Y. Cullens, M. E. Hervig, and J. M. Russell III (2014), Gravity wave activity during recent stratospheric sudden warming events from SOFIE temperature measurements, *J. Geophys. Res. Atmos.*, *119*, 8091–8103, doi:10.1002/2014JD021763.

Torrence, C., and G. P. Compo (1998), A practical guide to wavelet analysis, *Bull. Am. Meteorol. Soc.*, *79*(1), 61–78.

Trinh, Q. T., S. Kalisch, P. Preusse, M. Ern, H.-Y. Chun, S. D. Eckermann, M.-J. Kang, and M. Riese (2016), Tuning of a convective gravity wave source scheme based on HIRDLS observations, *Atmos. Chem. Phys.*, *16*, 7335–7356, doi:10.5194/acp-16-7335-2016.

Tsuchiya, C., K. Sato, M. J. Alexander, and L. Hoffmann (2016), MJO-related intraseasonal variation of gravity waves in the Southern Hemisphere tropical stratosphere revealed by high-resolution AIRS observations, *J. Geophys. Res. Atmos.*, *121*, 7641–7651, doi:10.1002/2015JD024463.

Tsuda, T., Y. Murayama, T. Nakamura, R. A. Vincent, A. H. Manson, C. E. Meek, and R. L. Wilson (1994), Variations of the gravity wave characteristics with height, season, and latitude revealed by comparative observations, *J. Atmos. Terr. Phys.*, *56*, 555–568.

Tsuda, T., M. Nishida, C. Rocken, and R. H. Ware (2000), A global morphology of gravity wave activity in the stratosphere revealed by the GPS occultation data (GPS/MET), *J. Geophys. Res.*, *105*(D6), 7257–7273, doi:10.1029/1999JD901005.

Vincent, R. A., and D. C. Fritts (1987), A climatology of gravity waves in the mesosphere and lower thermosphere over Adelaide, Australia, *J. Atmos. Sci.*, *44*, 748–760.

Wang, L., and M. J. Alexander (2010), Global estimates of gravity wave parameters from GPS radio occultation temperature data, *J. Geophys. Res.*, *115*, D21122, doi:10.1029/2010JD013860.

Wang, L., and M. A. Geller (2003), Morphology of gravity-wave energy as observed from 4 years (1998–2001) of high vertical resolution U. S. radiosonde data, *J. Geophys. Res.*, *108*(D16), 4489, doi:10.1029/2002JD002786.

Watanabe, S., Y. Kawatani, Y. Tomikawa, K. Miyazaki, M. Takahashi, and K. Sato (2008), General aspects of a T213L256 middle atmosphere general circulation model, *J. Geophys. Res.*, *113*, D12110, doi:10.1029/2008JD010026.

Wilson, R., M.-L. Chanin, and A. Hauchecorne (1991), Gravity waves in the middle atmosphere observed by Rayleigh lidar. Part 2. Climatology, *J. Geophys. Res.*, *96*, 5169–5183, doi:10.1029/90JD02610.

Wolter, K., and M. S. Timlin (2011), El Niño/Southern Oscillation behaviour since 1871 as diagnosed in an extended multivariate ENSO index (MEI.ext), *Int. J. Climatol.*, *31*, 1074–1087, doi:10.1002/joc.2336.

Wu, D. L. (2004), Mesoscale gravity wave variances from AMSU-A radiances, *Geophys. Res. Lett.*, *31*, L12114, doi:10.1029/2004GL019562.

Wu, D. L., and S. D. Eckermann (2008), Global gravity wave variances from Aura MLS: Characteristics and interpretation, *J. Atmos. Sci.*, *65*, 3695–3718.

Wu, D. L., and J. W. Waters (1996), Satellite observations of atmospheric variances: A possible indication of gravity waves, *Geophys. Res. Lett.*, *24*(24), 3631–3634, doi:10.1029/96GL02907.

Xu, J., A. K. Smith, R. L. Collins, and C.-Y. She (2006), Signature of an overturning gravity wave in the mesospheric sodium layer: Comparison of a nonlinear photochemical-dynamical model and lidar observations, *J. Geophys. Res.*, *111*, D17301, doi:10.1029/2005JD006749.

Yamashita, C., X. Chu, H.-L. Liu, P. J. Espy, G. J. Nott, and W. Huang (2009), Stratospheric gravity wave characteristics and seasonal variations observed by lidar at the South Pole and Rothera, Antarctica, *J. Geophys. Res.*, *114*, D12101, doi:10.1029/2008JD011472.

Yamashita, C., S. L. England, T. J. Immel, and L. C. Chang (2013), Gravity wave variations during elevated stratopause events using SABER observations, *J. Geophys. Res. Atmos.*, *118*, 5287–5303, doi:10.1002/jgrd.50474.

Yoshiki, M., and K. Sato (2000), A statistical study of gravity waves in the polar regions based on operational radiosonde data, *J. Geophys. Res.*, *105*, 17,995–18,011, doi:10.1029/2000JD900204.

Yue, J., L. Hoffmann, and M. J. Alexander (2013), Simultaneous observations of convective gravity waves from a ground-based airglow imager and the AIRS satellite experiment, *J. Geophys. Res. Atmos.*, *118*, 3178–3191, doi:10.1002/jgrd.50341.

Yue, J., S. D. Miller, L. Hoffmann, and W. C. Straka (2014), Stratospheric and mesospheric concentric gravity waves over tropical cyclone Mahasen: Joint AIRS and VIIRS satellite observations, *J. Atmos. Solar Terr. Phys.*, *119*, 83–90.

Yue, J., J. Russell III, Y. Jian, L. Rezac, R. Garcia, M. López-Puertas, and M. G. Mlynczak (2015), Increasing carbon dioxide concentration in the upper atmosphere observed by SABER, *Geophys. Res. Lett.*, *42*, 7194–7199, doi:10.1002/2015GL064696.

Zhang, Y., J. Xiong, L. Liu, and W. Wan (2012), A global morphology of gravity wave activity in the stratosphere revealed by the 8-year SABER/TIMED data, *J. Geophys. Res.*, *117*, D21101, doi:10.1029/2012JD017676.